13th International Conference on
Structural Health Monitoring of Intelligent Infrastructure
DOI: 10.3217/978-3-99161-057-1-142

Feasibility of micro-motion from SAR imagery for vibration-based SHM

Alessandro Lotti[1], https://orcid.org/0009-0000-5240-2122, Aleksanteri B. Vattulainen[2], https://orcid.org/0000-0003-1898-600X, Chiara Suppi[1], Sebastian Diaz Riofrio[2], Pietro Milillo[3,4], Enrico Tubaldi[2], Daniele Zonta[1], Carmine Clemente[2]

[1] Department of Civil, Environmental and Mechanical Engineering, University of Trento, Trento, Italy
[2]Department of Electronic and Electrical Engineering, University of Strathclyde, Glasgow, UK
[3]Department of Civil and Environmental Engineering, University of Houston, Houston, TX, USA
[4]Visiting Scientist, German Aerospace Center, Munich, Germany
email: alessandro.lotti@unitn.it

ABSTRACT: This paper explores the use of single-pass Synthetic Aperture Radar (SAR) images to remotely measure the vibrational response of reflective ground targets, aiming to support vibration-based Structural Health Monitoring (SHM) of civil infrastructure. A Sub-Pixel Offset Tracking (SPOT) technique is applied to SAR imagery to reconstruct the time history of radial velocity, using the principle of micro-motion (m-m) effects induced by vibrating targets. Validation is by comparing SAR-extracted velocity profiles with synchronous ground measurements of a vibrating Corner Reflector (CR). Three representative test cases— including single-frequency, and amplitude-modulated vibrations—with maximum displacement values of 24.1 mm, 1.1 mm and 0.5 mm are analyzed using SAR images collected by the Umbra X-band SAR constellation. The extracted vibrational features are evaluated through time-domain correlation, spectral accuracy, and error metrics. Results confirm that SPOT can reconstruct velocity time histories and frequency content reliably for medium-to-high velocity scenarios (> 10 mm/s) and single-frequency signals. Even under low-velocity, complex signal conditions, the main frequency peaks are detectable, with negligible frequency errors and correlations of 0.61 (time) and 0.82 (frequency). This study demonstrates the potential of SAR m-m processing for fully remote vibration-based SHM, offering a scalable, installation-free alternative for assessing structural dynamics.

KEY WORDS: Structural Health Monitoring, Remote sensing, SAR-Imaging, Micro-Motion, Micro-Doppler, Modal Analysis.

1 INTRODUCTION

1.1 Background

Structural Health Monitoring (SHM) traditionally relies on contact-based sensors such as accelerometers to detect changes in a structure dynamic response [1]. While its claimed effectiveness in extracting the modal parameters – such as natural frequencies, damping ratios and modeshapes – they often face limitations in terms of costs, installation complexity, and sensor coverage [2], especially for large civil infrastructure. The need for prompt, scalable, and contactless sensing has led to increasing interest in remote sensing technologies [3]. Among these, spaceborne Synthetic Aperture Radar (SAR) stands out. SAR uses radar signals emitter from a sensor mounted on a satellite, to create images of the Earth surface. A SAR image appears as a complex matrix in range and azimuth coordinates, range corresponding to the radial direction (sensor to ground target) and azimuth to the direction of velocity of the platform (e.g., the satellite) motion [4].

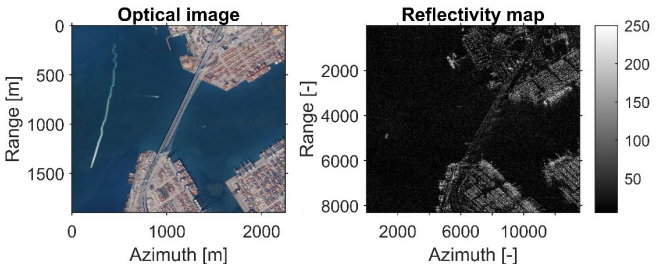

Figure 1.1. SAR image (from Umbra Sensor [5]) reflectivity map of the Stonecutters Bridge (Hong Kong harbor) compared to its optical image.

SAR has gained considerable attention thanks to its ability to cover large areas – ranging from 5 km to 200 km in width [6], [7] – and to detect ground movement through Interferometric SAR (InSAR), which reconstructs displacement trends by combining multiple images of the same area acquired over time [8]. Whilst InSAR is a widely recognized technique for measuring millimetric precision displacements [9], it requires a large dataset [10] and cannot extract SHM-related information from a single pass (i.e., single image). In contrast, recent literature shows that it is possible to overcome these limitations of InSAR and use single-pass SAR images to extract vibrational information from reflective ground targets, through different techniques based on the measurement of micro-motions (m-m) using the micro-Doppler (m-D) phenomenon [11].

1.2 Micro-motion in SAR images

In a SAR image, each pixel contains magnitude (reflectivity) and phase information. Targets with strong reflectivity, such as metallic objects with sharp geometries, are prominently visible in the reflectivity map. Figure 1.1 shows an example of a reflectivity map alongside its corresponding optical image of the Stonecutters Bridge in Hong Kong.

The spatial resolution of the SAR image – defined as the size of each pixel in meters along the range and azimuth directions – depends on several factors, particularly the acquisition time (t_a) in the azimuth direction. Acquisition time refers to the duration over which the satellite observes the same ground target, from the start to the end of the collection. This duration can vary significantly depending on the type of satellite sensor and the acquisition mode employed.

DOI: 10.3217/978-3-99161-057-1-142

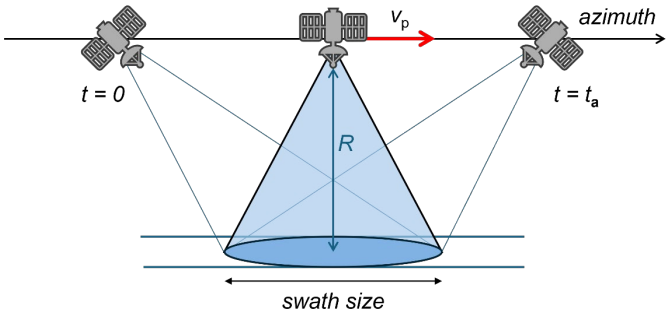

Figure 1.2. SAR acquisition geometry in case of spotlight acquisition mode.

In this work, SAR imagery collected in spotlight mode is studied. In this acquisition mode, the radar beam is continuously steered (or "squinted") to remain focused on the same ground area for an extended duration – typically between 5 and 20 seconds – greatly improving azimuth resolution. An example of the geometry of the SAR collection is shown in Figure 1.2. For spotlight acquisitions, the azimuth resolution Δx is given by Eq. (1):

$$\Delta x = \frac{\lambda R}{2 v_p t_a} \quad (1)$$

where λ is the wavelength of the SAR sensor (typically 25-40 mm for X-band radars), R is the radial distance to the ground target, v_p is the platform (satellite) velocity in the azimuth direction, and t_a is the acquisition duration (or illumination time). When generating a SAR image, the scene is typically assumed to be static – i.e., objects still on the surface. However, when a target is moving, its position in the image will be shifted in the range-azimuth plane due to uncompensated signal phase shift associated with the motion (imparted by the Doppler effect), causing a defocusing and smearing of the object. A point moving at constant speed, will be displaced mainly in the azimuth direction by a distance governed by Eq. (2) [12]:

$$x = \frac{v_r R}{v_p} \quad (2)$$

where v_r is the radial velocity of the object, R is the radial distance to the ground target, and v_p is the platform velocity in the azimuth direction. Since it is the change in radial velocity v_r relative to the moving satellite that produces this effect, the radial velocity is the key quantity of interest in this study.

Micro-motions of a target, such as vibrations, cause periodic fluctuations in the radar signal frequency due to the Doppler effect, where this is specifically referred to as micro-Doppler (m-D) [13]. In SAR imagery, this effect results in the formation of paired echoes along the azimuth direction around the real target [14], as shown in Figure 1.3. These effects are visible in the reflectivity image and can be exploited to measure the vibrations of reflective ground targets. The faster the velocity of vibration, the more evident these echoes appear.

The earliest studies in this field, such as [15], explored how to extract vibrations and rotations from moving targets. Later works investigated the potential of employing this principle for SHM in civil engineering, applying it to a dam and a bridge, respectively [11], [16].

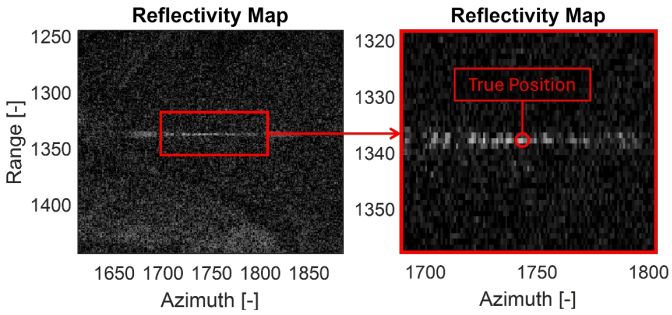

Figure 1.3. Micro-Doppler from an isolated target, vibrating vertically with an amplitude of 45 mm and frequency 0.8 Hz.

1.3 Research objective

The objective of this work is to assess the feasibility of using single-pass SAR images to extract vibration characteristics (i.e. micro-motions) from isolated reflective targets. Specifically, the performance and limitations of the extraction technique are assessed under different conditions of target vibrational amplitude, frequency, and movement time history complexity. Three representative test scenarios are used, and synchronous ground truth measurements are used as validation benchmarks.

The paper is structured as follows: Section 2 introduces the algorithm used to implement the m-m SAR method. Section 3 provides an overview of the experimental validation setup and the SAR datasets employed. Section 4 presents the results along with a detailed discussion. Lastly, Section 5 reports conclusions and summarizes the key insights of the study.

2 METHODOLOGY

2.1 Sub-Pixel Offset Tracking (SPOT)

The m-m SAR technique uses single-pass SAR imagery to estimate the radial velocity time history of a ground target within the observation window of the SAR image. The core algorithm used for this purpose is the Subpixel-Offset-Tracking (SPOT), as the one used in [11] and [16]. After cropping the area around the target (Region of Interest – ROI), SPOT segments the SAR image (full-aperture), into N sub-images (sub-apertures), each focused from a fraction of the full image observation time. To achieve this, a Fast Fourier Transform (FTT) is performed on the ROI along the azimuth dimension to convert the data from *range versus azimuth* to *range versus azimuth-frequency*. A segmentation in sub-apertures along the azimuth frequency axis is then performed using window lengths defined by the aperture fraction α (see Figure 2.1):

$$\alpha = \frac{t_{sap}}{t_a} \quad (3)$$

where t_{sap} represents the duration in time of the sub-aperture, and t_a the acquisition duration (full aperture). Adjacent sub-apertures can share portions of the azimuth frequency domain (and therefore time); as controlled by the overlap ratio Ω:

$$\Omega = \frac{t_{ol}}{t_{sap}} \quad (4)$$

where t_{ol} is the overlap duration between adjacent sub-apertures.

DOI: 10.3217/978-3-99161-057-1-142

Given α and Ω, the total number of sub-apertures N can be computed as:

$$N = \frac{\alpha^{-1} - \Omega}{1 - \Omega} \tag{5}$$

The N *azimuth-frequency* sub-apertures are individually transformed into to N *range versus azimuth* images by means of an Inverse FFT. The target azimuth displacement x is then tracked across the sequence of sub-apertures using 2D cross-correlation. Each target azimuth shift x_k – given a specific k-th sub-aperture – depends on the instantaneous value of the radial velocity $v_{r,k}$. Therefore, it is possible to invert Eq. (2) to obtain the value of the radial velocity given the azimuth shift x_k:

$$v_{r,k} = \frac{x_k v_p}{R} \tag{6}$$

The time vector associated with the reconstructed velocity is a linearly spaced sequence of N values, starting at $t_{sap}/2$ and ending at $t_a - t_{sap}/2$. The temporal resolution is then given by:

$$\Delta t = \frac{t_a - t_{sap}}{N-1} \tag{7}$$

To ensure the desired frequency content is captured by the time series, the sampling frequency must satisfy the Nyquist criterion for the maximum frequency, f_{max}, to be observed:

$$f_s = \frac{1}{\Delta t} \geq f_{max} \tag{8}$$

There are two main ways to increase the sampling frequency: reduce the aperture fraction α, or increase the overlap ratio Ω. It should, however, be noted that reducing the aperture fraction shortens the illumination time for each sub-aperture and consequently worsens the azimuth resolution of each sub-aperture image. When the aperture fraction becomes too small, the target may no longer appear as a distinct feature, thereby degrading the tracking performance. This imposes a practical limit on how finely the aperture can be segmented, although this can be mitigated by increasing the overlap.

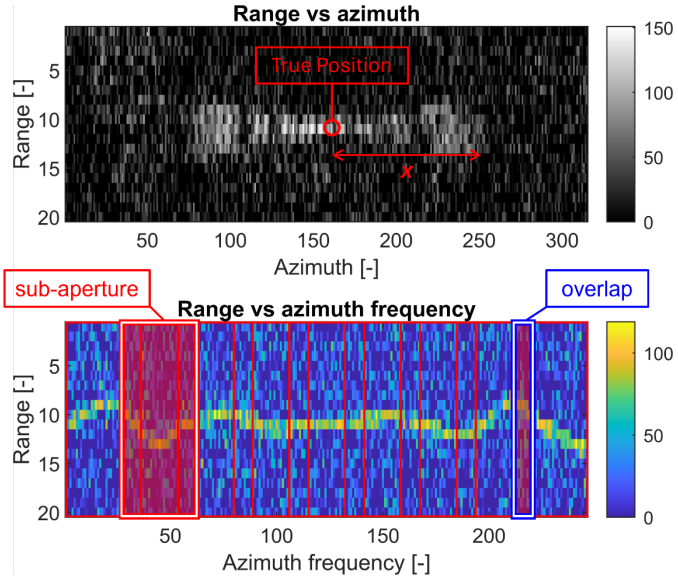

Figure 2.1. Top: range versus azimuth ROI (with highlighted and the azimuth shift x); bottom: FFT of ROI along azimuth, yielding range versus azimuth frequency data, with the segmentation of sub-aperture data indicated.

The fundamental steps of the SPOT algorithm are as follows:

1. Crop the SAR image around the ROI;
2. Apply an FFT along azimuth to convert the ROI to the *range versus azimuth-frequency* domain;
3. Segment the azimuth-frequency spectrum into N sub-apertures according to selected parameters α and Ω;
4. Apply IFFT to obtain N range versus azimuth sub-aperture images;
5. Track the azimuth pixel displacement of the target across sub-apertures;
6. Compute the velocity and the associated time-vector.

3 EXPERIMENTAL VALIDATION

3.1 Tests sites and ground instrumentation

To evaluate the effectiveness of the m-m SAR technique, controlled experiments were conducted using artificially vibrating targets with ground truth data measured synchronously with the satellite passage. Tests took place in open fields in Trento, Italy, and Glasgow, UK, to avoid interference from nearby objects (see Figure 3.1).

The instrumentation setup included a Corner Reflector (CR) mounted on a shaker device, with motion captured using a Linear Variable Displacement Transducer (LVDT) (see Figure 3.2). The sensor recorded vertical displacement at a sampling rate of 50 Hz, where this was later projected onto the satellite radial direction and synchronized to match the satellite passage. As the m-m SAR algorithm measures velocity rather than displacement, the ground displacement signals were numerically differentiated to obtain the synchronized radial velocity profiles. This allowed for a direct comparison between SAR measured velocities and ground truth data. This study focuses on three representative test configurations, summarized in Table 1. The shaker was set to simulate various amplitudes and types of vibrational signals, including single-frequency sinusoidal oscillations and amplitude-modulated waveforms. In the context of civil engineering, the amplitude of structural vibrations can vary considerably depending on the structural type. For long-span bridges, typical displacements range from 0.1 mm to 5 mm, corresponding to radial velocities of approximately 1–10 mm/s or lower. To replicate these conditions, the test campaign was designed to progressively study vibrations beginning with well-defined, high-amplitude motions to those of lower-amplitude more relevant to SHM of bridges. The maximum target velocities for Tests 1, 2, and 3 were 95.5 mm/s, 10.8 mm/s, and 3.1 mm/s, respectively, corresponding to peak vertical displacements of 24.1 mm, 1.1 mm, and 0.5 mm.

To refine the analysis, the SAR measured velocity time histories were fitted using a model based on the superposition of multiple sinusoidal components. First, the SAR velocity spectra were upsampled by a factor of four, and dominant frequencies were identified from the FFT. For Tests 1 and 2, the frequency corresponding to the primary peak was selected, while for Test 3, being amplitude modulated, the three most dominant frequency components were extracted. These extracted frequencies were then used to fit sinusoidal models by optimizing amplitude and phase only. This procedure allowed for the reconstruction of refined, high-resolution velocity time histories.

DOI: 10.3217/978-3-99161-057-1-142

3.2 SAR acquisitions

Satellite data were collected by the Umbra X-band SAR constellation, capable of high-resolution spotlight-mode imaging. Spotlight acquisition was selected to maximize the collection time, and therefore the azimuth resolution.

Commonly, SAR providers deliver Multi-Look Complex (MLC) images, which are generated by averaging multiple looks in the azimuth and/or range directions from the same observation in order to reduce speckle noise. While this averaging improves image interpretability, it also reduces the effective resolution (due to lower acquisition time) and suppresses the micro-motion effects (i.e., paired echoes), that are critical to this study. To preserve these effects, images were provided by Umbra in the form of Single-Look Complex (SLC) products, containing a single, unaveraged observation in both range and azimuth directions. These were processed using the polar format algorithm.

The three SAR images were acquired using sensors operating at a central frequency of 9.6 GHz, corresponding to a wavelength of $\lambda = 31$ mm. The main characteristics of the SAR acquisitions used in the three tests are summarized in Table 1.

3.3 Evaluation of the performance

The ground-measured radial velocities served as a validation benchmark to quantify the performance of SPOT in reconstructing the time history of radial velocity of the target, during the SAR acquisition. To achieve this, the accuracy was evaluated according to the following metrics:

- Root Mean Square of the Error ($RMSE$), computed in the time domain by comparing the SAR-reconstructed and ground-measured velocities at matching timestamps.
- Frequency error (ϵ_f), evaluated as the residual between the true frequency and the frequency measured with m-m SAR, corresponding to the highest peak of the FFT;
- Correlation in time (ρ_t) and frequency (ρ_f) domains.

Table 1. Test configurations. The table reports: type of signal tested (Signal type), principal frequency of vibration (f), maximum ground vertical displacement ($d_{\max}$), maximum radial velocity value ($v_{r,\max}$), SAR sensor name (Sensor), Pulse Repetition Frequency (PRF), acquisition duration (t_a), incidence angle (θ), platform velocity (v_p), slant-range distance (R), range resolution (Δx), and azimuth resolution (Δx).

Quantity	Test	1	2	3
Signal type	[-]	SIN	SIN	AM
f	[Hz]	1	2	1
$d_{\max}$	[mm]	24.1	1.1	0.5
$v_{r,\max}$	[mm/s]	95.5	10.8	3.1
Date	[d/m/y]	18/11/23	14/03/24	30/01/25
Time UTC	[H:M:S]	20:46:27	21:29:22	10:46:27
PRF	[kHz]	5.75	6.31	7.75
t_a	[s]	6.04	5.95	14.70
θ	[°]	54.8	49.4	34.5
v_p	[km/s]	7.69	7.67	7.65
R	[km]	844	795	683
Δy	[mm]	0.18	0.17	0.13
Δx	[mm]	0.22	0.21	0.07

(a) (b)

Figure 3.1. Tests Locations in (a) Trento, Italy; and (b) Glasgow, UK.

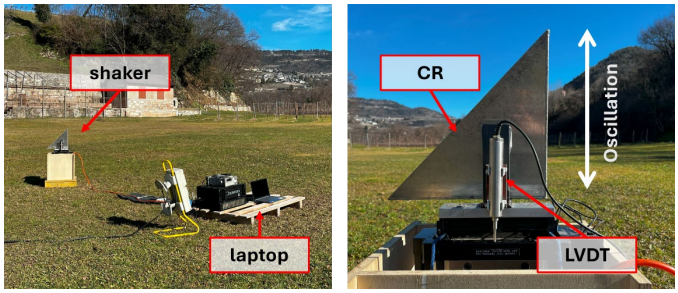

(a) (b)

Figure 3.2. Instrumentation employed: (a) shaker and acquisition system, (b) Detail of CR and LVDT.

4 RESULTS AND DISCUSSION

This section highlights the results of the SPOT m-m measurement technique, as well as the performance evaluation through the comparison with ground data. The comparison is performed both graphically (see Figure 4.1, Figure 4.2, Figure 4.3) and numerically (Table 2), using error metrics such as $RMSE$, frequency error, and Pearson's correlation coefficients in time and frequency domains. Results focus on Tests 1, 2, and 3 as representative cases for varying vibration conditions. Each test was processed using the workflow described in Section 2, with extraction parameters summarized in Table 2.

Table 2. Metric results. The table reports for each test: maximum radial velocity value ($v_{r,\max}$), acquisition duration (t_a), aperture fraction (α), overlap ratio (Ω), number of sub-apertures (N), sampling frequency (f_s), frequency resolution (Δf), $RMSE$ and $RMSE$ relative to max velocity value ($RMSE\%$), frequency residual error (ϵ_f), correlations in time (ρ_t) and frequency (ρ_f) domains for the raw m-m SAR signal.

Quantity	Test	1	2	3
$v_{r,\max}$	[mm/s]	95.5	10.8	3.1
t_a	[s]	6.04	5.95	14.70
α	[%]	7.6	4.3	4.5
Ω	[%]	35	40	49
N	[-]	23	38	42
t_{sap}	[s]	0.46	0.27	0.66
f_s	[Hz]	3.23	6.49	2.92
Δf	[Hz]	0.18	0.18	0.07
$RMSE$	[mm/s]	30.4	6.7	1.2
$RMSE\%$	[%]	31.8	62.0	38.7
ϵ_f	[Hz]	0.03	0.06	0.02
ρ_t	[-]	0.89	0.65	0.66
ρ_f	[-]	0.98	0.79	0.71

DOI: 10.3217/978-3-99161-057-1-142

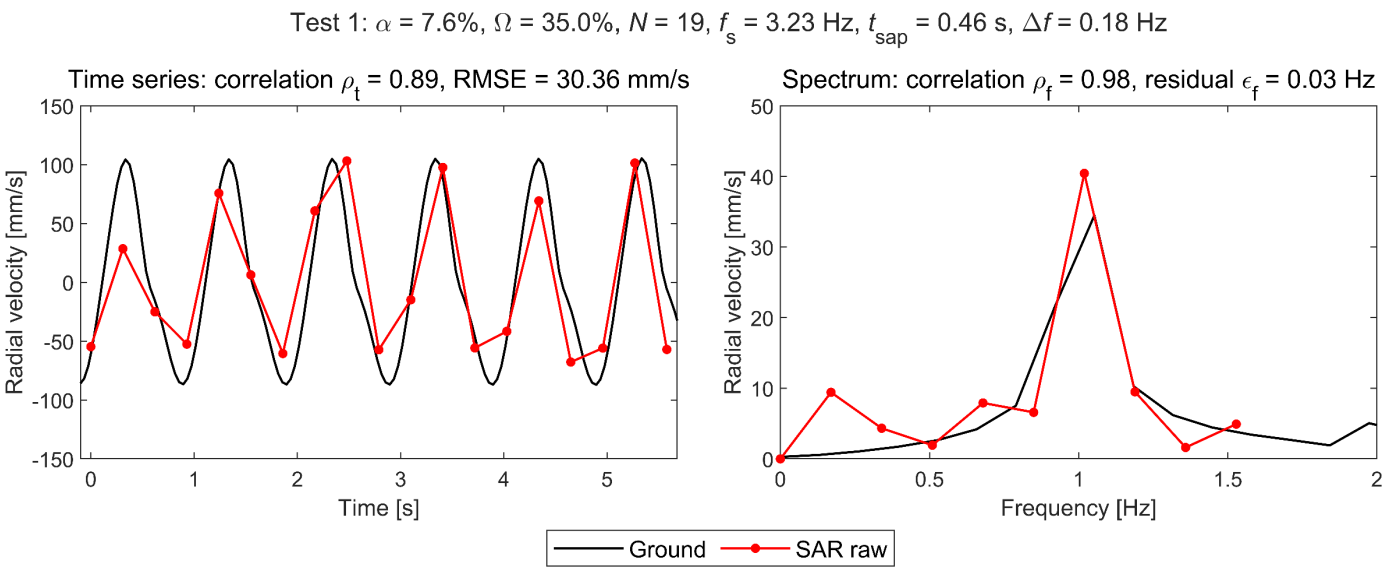

Figure 4.1. Test 1: results and comparison with ground data.

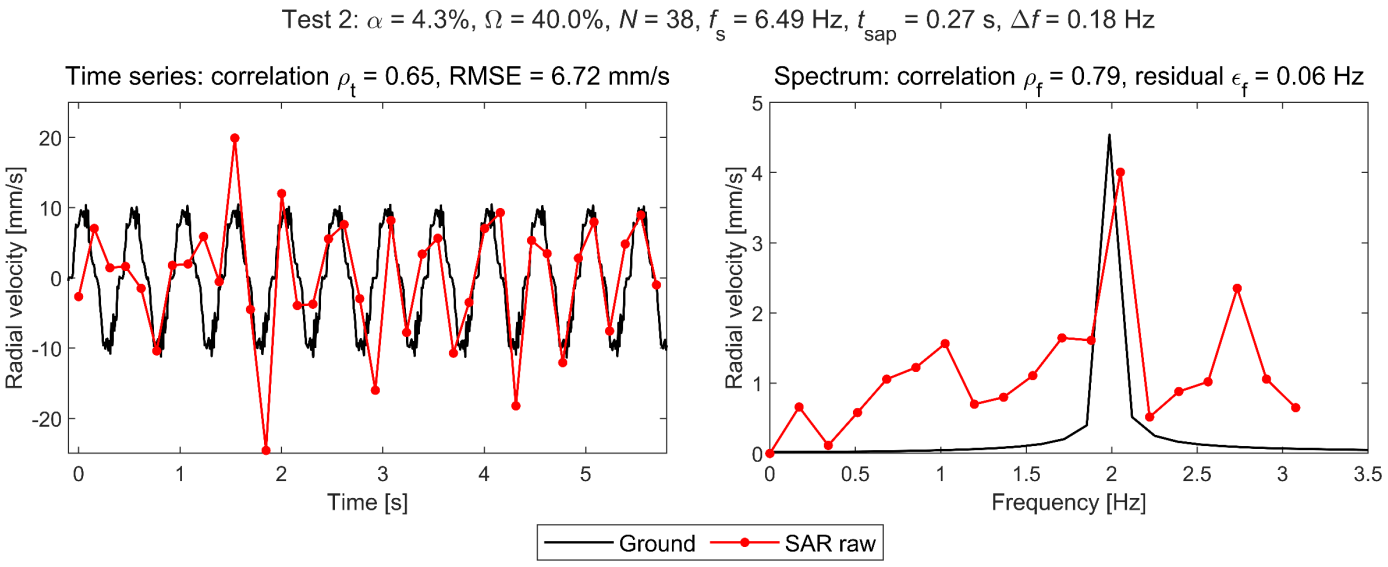

Figure 4.2. Test 2: results and comparison with ground data.

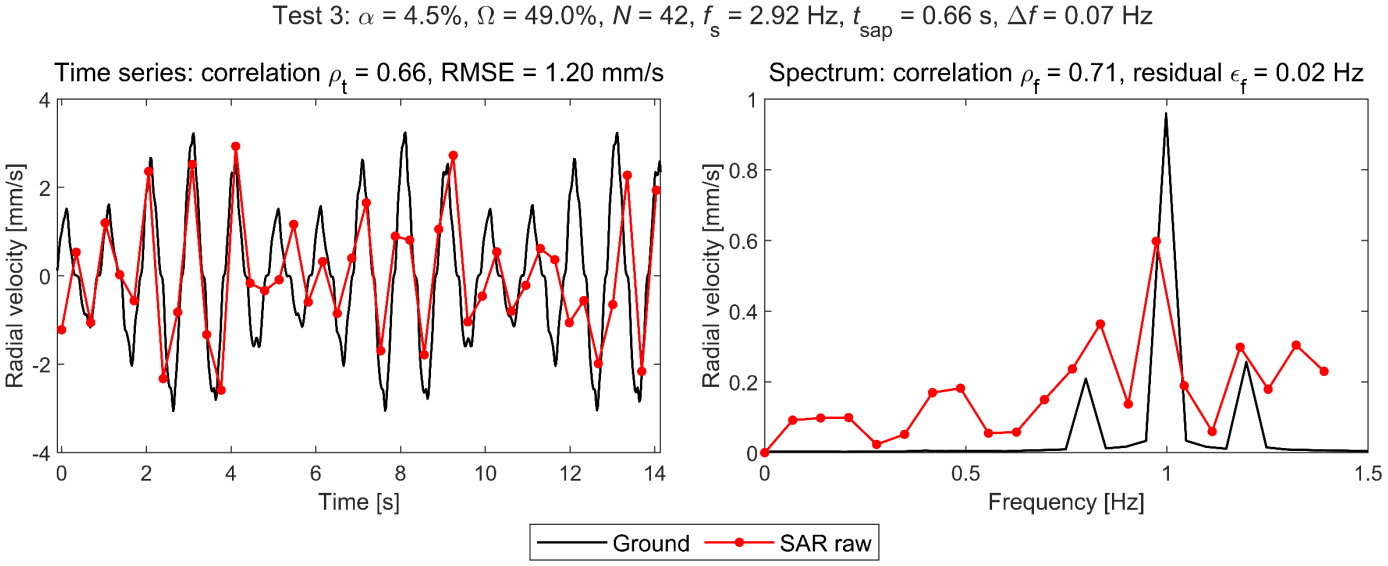

Figure 4.3. Test 3: results and comparison with ground data.

DOI: 10.3217/978-3-99161-057-1-142

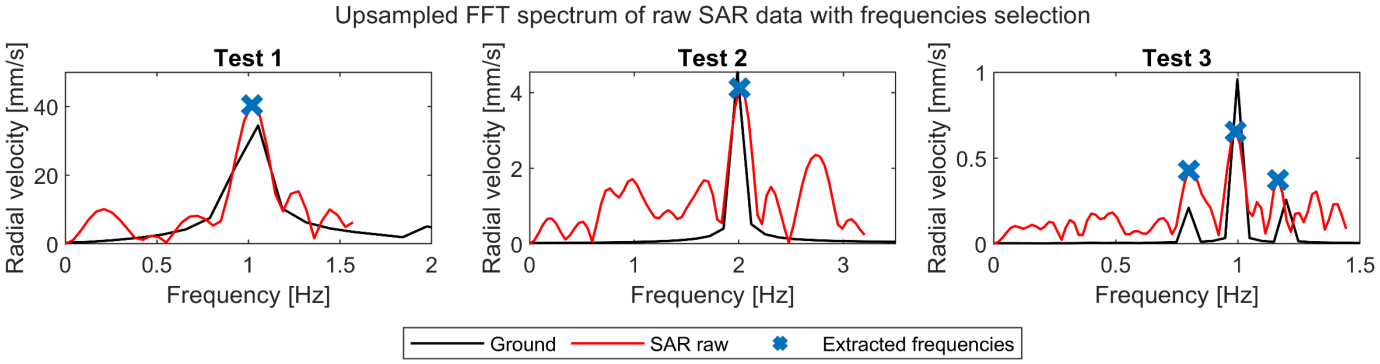

Figure 4.4. Upsampled SAR FFT spectra compared to ground truths. Plots shows the most dominant frequencies extracted.

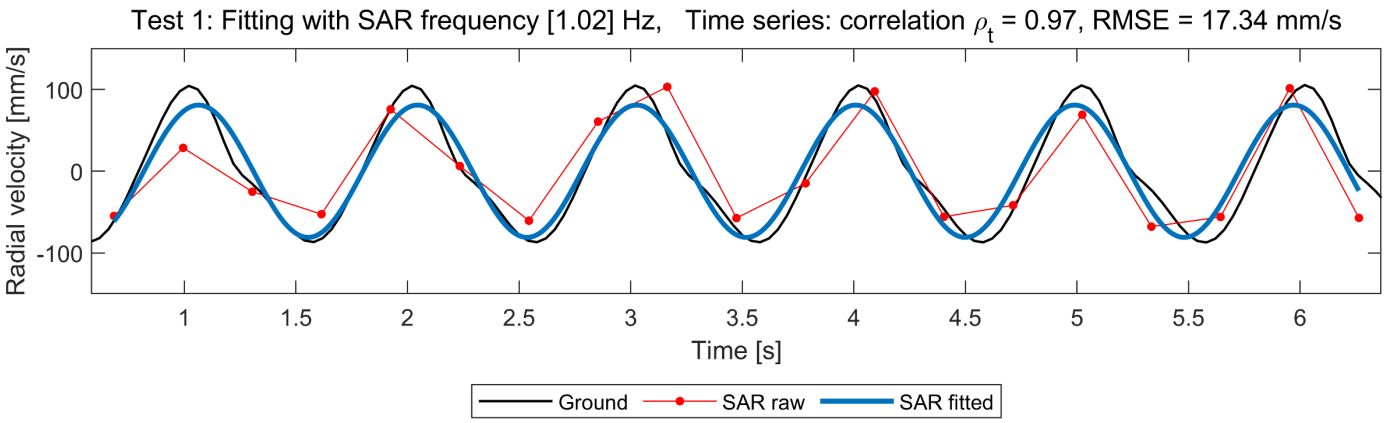

Figure 4.5. Test 1: results of model fitting on the SAR measurement, using a frequency of 1.02 Hz.

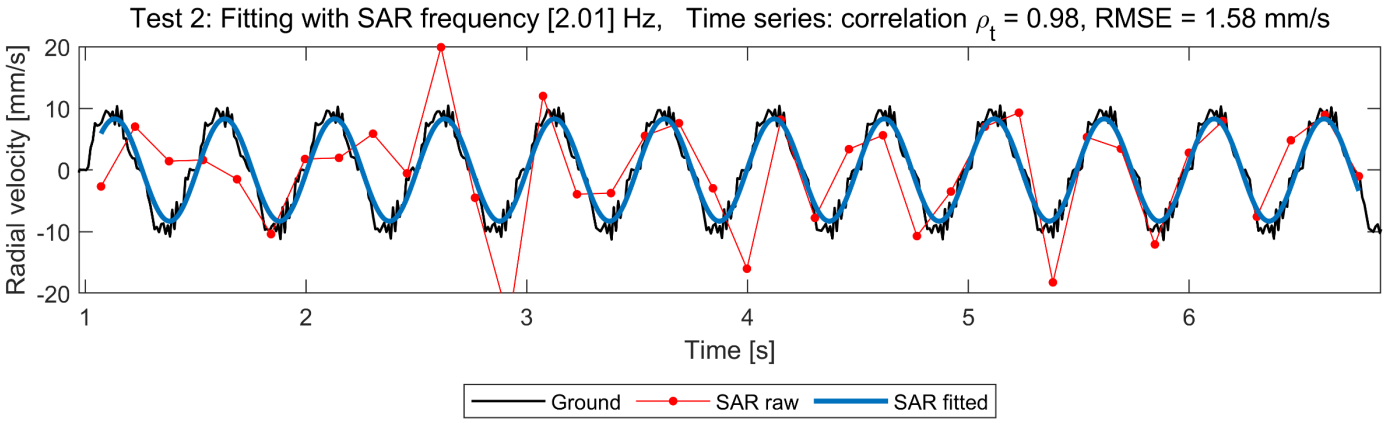

Figure 4.6. Test 2: results of model fitting on the SAR measurement, using a frequency of 2.01 Hz.

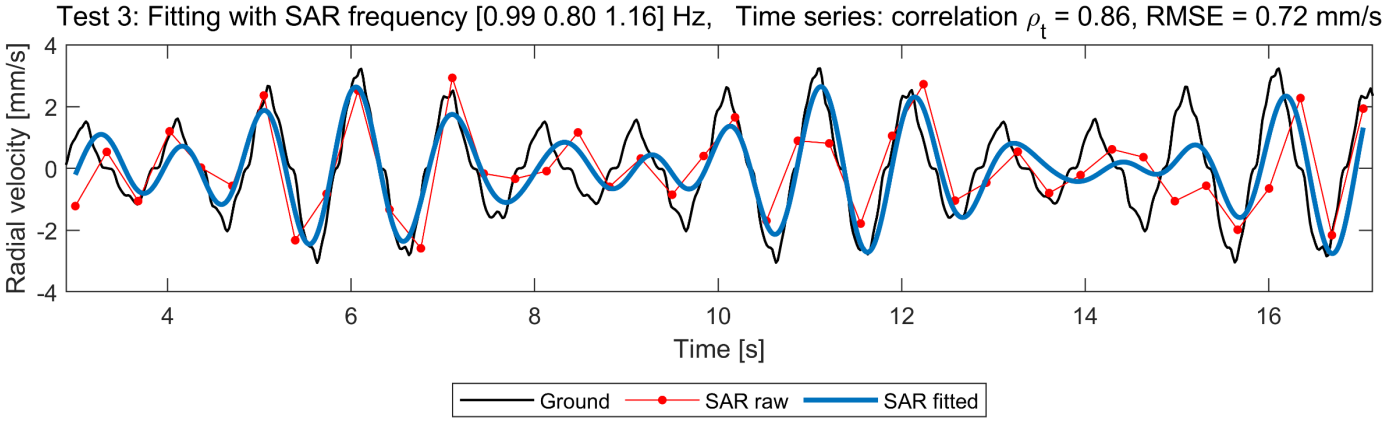

Figure 4.7. Test 3: results of model fitting on the SAR measurement, using frequencies of 0.80 Hz, 0.99 Hz, 1.16 Hz.

DOI: 10.3217/978-3-99161-057-1-142

4.1 Test 1 – High-velocity, single-frequency vibration

Test 1, presented in Figure 4.1, features the simplest case, with a low single-frequency oscillation (1 Hz) and relatively high vibration velocity ($v_{r,\max}$ = 95.5 mm/s). The parameters to obtain the best extraction possible were an aperture fraction α = 7.6% and overlap ratio Ω = 43%, resulting in a sub-aperture duration of t_{sap} = 0.39 s and sampling rate of f_{s} = 3.23 (well above the Nyquist rate for the frequency of interest, 1 Hz). The limited acquisition time led to a spectral resolution of Δf = 0.18 Hz. The extracted signal closely matches the ground truth in both time and frequency domains, proved by high Pearson's correlation coefficients, with ρ_t = 0.89 and ρ_f = 0.98 for time and frequency, respectively.

The dominant vibration frequency is accurately identified with frequency residual error of ϵ_f = 0.03 Hz (lower than the frequency resolution), as well as a correct estimation of the amplitude of the peak in the frequency spectrum. The RMSE in the extraction of the velocity time history is 30.4 mm/s (corresponding to a 31.8% relative to the true peak velocity value).

4.2 Test 2 – Mid-velocity, single-frequency vibration

Test 2, shown in Figure 4.2, presents another constant frequency extraction, however with a frequency of 2 Hz and a vibration amplitude reduced by an order of magnitude to $v_{r,\max}$ = 10.8 mm/s, making it a more challenging case. Here, the aperture fraction α was decreased to 4.3%, and the overlap ratio Ω set to 40%, resulting in a sub-aperture duration t_{sap} of 0.27 seconds and a sampling rate f_{s} of 6.49 Hz.

The main frequency component is correctly identified, being the error ϵ_f = 0.06 Hz (lower than the resolution Δf = 0.18 Hz). Some local discrepancies appear in the time-domain signal, including underestimation and overestimation of peak values. Despite the lower absolute RMSE (6.7 mm/s), the relative error is 62.0% due to the lower ground truth amplitude. The time-domain correlation decreases significantly due to the impact of measurement noise, with ρ_t = 0.65, while frequency domain correlation remains satisfactory at ρ_f = 0.79. The spectrum also shows minor spurious peaks at 1 Hz and 2.7 Hz.

4.3 Test 3 – Low-velocity, amplitude-modulated vibration

Test 3, represented in Figure 4.3, involved a more complex amplitude-modulated signal with significantly lower velocity magnitude of $v_{r,\max}$ = 3.1 mm/s, which is more representative of vibrations from long span bridges or viaducts. An aperture fraction α of 4.5% and an overlap ratio Ω = 49% were used. This configuration resulted in a sub-aperture duration of 0.66 seconds and a sampling frequency of f_{s} = 2.92 Hz. In this case spectral resolution was finer, of 0.07 Hz, thanks to the longer acquisition time.

Despite the reduced signal energy, the algorithm extracts the carrier frequency, with a low residual error of ϵ_f = 0.02 Hz (within the frequency resolution Δf = 0.07 Hz) and a frequency domain correlation ρ_f = 0.71 – both comparable to Test 2. Time domain correlation is satisfactory at ρ_t = 0.66, while the RMSE for this extraction is 1.2 mm/s, with a relative error of 38.7%, the latter being more comparable to Test 1. This suggests that the dominant frequency of vibration has an impact on the quality of the extraction.

4.4 SAR data fitting

Fitting the SAR-extracted data significantly improved the quality of the time-domain signal, both visually and quantitatively. As shown in Figures 4.5, 4.6, and 4.7, temporal resolution was enhanced through model-based fitting without altering the extraction parameters α or Ω. For each test, the dominant frequency components were identified from the upsampled FFT (upsampling factor = 4), and a sum of sinusoids with those frequencies was then fitted to the SAR data by optimizing only amplitude and phase. Results are as follows:

- *Test 1*: From the upsampled FFT, a frequency of 1.02 Hz was extracted. A single sinusoid was fitted, yielding an RMSE improvement from 30.34 to 17.34 mm/s, and a time-domain correlation increase from 0.89 to 0.97.
- *Test 2:* The extracted frequency was 2.01 Hz. After fitting, RMSE dropped from 6.72 to 1.58 mm/s, and ρ_t improved from 0.79 to 0.98.
- *Test 3*: Multiple dominant frequencies were identified at 0.80, 0.99, and 1.16 Hz. Fitting a sum of three sinusoids led to an RMSE reduction from 1.20 to 0.72 mm/s, and a correlation increase from 0.76 to 0.86.

These results demonstrate that using prior knowledge about the expected oscillatory behavior can significantly enhance the extraction quality. By narrowing the solution space to plausible signal shapes, fitting allows more accurate recovery of the target vibration profile.

5 CONCLUSIONS

This paper presented a feasibility study on the use of single-pass SAR images for extracting vibration characteristics from oscillating ground targets via the Sub-Pixel Offset Tracking (SPOT) micro-motion measurement technique. The algorithm was validated through a series of experimental tests, involving an isolated moving Corner Reflector (CR). The performance of the technique was assessed against synchronously acquired ground truth data.

Results demonstrate that SPOT can accurately reconstruct vibration-based information, capturing the dominant frequencies of motion with frequency errors well under the spectral resolution, even under varying conditions of signal amplitude, frequency, and complexity. The algorithm is also able to reconstruct the time histories of radial velocity with correlation values ranging from 0.65 to 0.98 (for the worst case, and best extraction case, respectively) and relative errors RMSE% from 31.8% to 62.0%. For high-velocity, single-frequency oscillations, SPOT achieves excellent correlation with ground truth in both time and frequency domains, respectively at 0.88 and 0.95, with relative RMSE values below 32%. When applied to more challenging low-velocity and amplitude-modulated cases, the method still proves effective in detecting the carrier frequency (with frequency correlations spanning 0.71 to 0.79) and producing meaningful velocity profiles, although the quality declines as vibration velocity decreases, and as frequency content becomes more complex.

Using prior knowledge about the expected oscillatory behavior can significantly enhance the extraction quality. Results from model fitting feature a significant reduction in RMSE and an improvement in correlation, even for the lowest velocity amplitude modulated case, improving from 1.20 mm/s to 0.72 mm/s (with a correlation increase from 0.66 to 0.86).

DOI: 10.3217/978-3-99161-057-1-142

Limitations concerning m-m SAR measurements are primarily attributed to SAR acquisition constraints, such as short acquisition time, noise and image clutter. Alternative processing strategies could be explored to overcome these issues, particularly those using the phase information rather than the reflectivity. Additionally, the noise-affected velocity profile, in combination with limited acquisition durations, limits the application of m-m SAR for time domain modal extractions, to reconstruct not only the natural frequency but possibly the modeshapes and damping coefficients. On the other hand, the algorithm proves to be quite effective for extracting the frequency spectrum.

Despite these challenges, the study confirms that SAR m-m measurement opens new possibilities for remote vibration-based SHM. Future work will focus on refining the methodology by optimizing the extraction parameters, integrating phase-domain information, improving noise suppression models, and validating the algorithm on real-world bridge structures.

ACKNOWLEDGMENTS

The study presented was funded by: the European Space Agency under the projects “Bridge Monitoring Based on Single Pass SAR Images” and “EO4Security- Innovative SAR Processing Methodologies For Security Applications-Topic B2: Micro-Doppler Processing”, the ReLUIS Interuniversity Consortium under the agreement DPC-ReLUIS 2020-2022 and DPC-ReLUIS 2024-2026 WP 6 “Monitoring and satellite data”, and the European Union- Next Generation EU, Mission 4 Component 2 - CUP E53D23003560006.

The authors would also like to acknowledge the collaboration of Umbra for providing satellite images, the Glasgow City Council for authorizing on-site tests., and the University of Trento and the University of Strathclyde for helping with the tests.

REFERENCES

[1] Wei Fan and Pizhong Qiao, ‘Vibration-based Damage Identification Methods: A Review and Comparative Study’, *Struct. Health Monit.*, vol. 10, no. 1, pp. 83–111, Jan. 2011, doi: 10.1177/1475921710365419.

[2] J. M. W. Brownjohn, ‘Structural health monitoring of civil infrastructure’, *Philos. Trans. R. Soc. Math. Phys. Eng. Sci.*, vol. 365, no. 1851, pp. 589–622, Feb. 2007, doi: 10.1098/rsta.2006.1925.

[3] A. Mardanshahi, A. Sreekumar, X. Yang, S. K. Barman, and D. Chronopoulos, ‘Sensing Techniques for Structural Health Monitoring: A State-of-the-Art Review on Performance Criteria and New-Generation Technologies’, *Sensors*, vol. 25, no. 5, p. 1424, Feb. 2025, doi: 10.3390/s25051424.

[4] N. Earth Science Data Systems, ‘Synthetic Aperture Radar (SAR) | NASA Earthdata’. Accessed: Apr. 17, 2025. [Online]. Available: https://www.earthdata.nasa.gov/learn/earth-observation-data-basics/sar

[5] Umbra Space, ‘Delivering Global Omniscience • Umbra’. Accessed: Jan. 22, 2025. [Online]. Available: https://umbra.space/

[6] ‘Copernicus: Sentinel-1 - eoPortal’. Accessed: Apr. 17, 2025. [Online]. Available: https://www.eoportal.org/satellite-missions/copernicus-sentinel-1

[7] ‘Umbra SAR Constellation - eoPortal’. Accessed: Apr. 17, 2025. [Online]. Available: https://www.eoportal.org/satellite-missions/umbra-sar#orbit

[8] A. Ferretti, C. Prati, and F. Rocca, ‘Permanent scatterers in SAR interferometry’, *IEEE Trans. Geosci. Remote Sens.*, vol. 39, no. 1, pp. 8–20, Jan. 2001, doi: 10.1109/36.898661.

[9] D. Tonelli, A. Valentini, A. Rocca, S. Zorzi, A. Lotti, and D. Zonta, ‘Uncertainty quantification of satellite InSAR-monitoring of bridges: a case study’, *ce/papers*, vol. 6, no. 5, pp. 900–906, Sep. 2023, doi: 10.1002/cepa.1991.

[10] D. Perissin, ‘Interferometric SAR Multitemporal Processing: Techniques and Applications’, in *Multitemporal Remote Sensing*, vol. 20, Y. Ban, Ed., in Remote Sensing and Digital Image Processing, vol. 20. , Cham: Springer International Publishing, 2016, pp. 145–176. doi: 10.1007/978-3-319-47037-5_8.

[11] F. Biondi, P. Addabbo, S. L. Ullo, C. Clemente, and D. Orlando, ‘Perspectives on the Structural Health Monitoring of Bridges by Synthetic Aperture Radar’, *Remote Sens.*, vol. 12, no. 23, p. 3852, Nov. 2020, doi: 10.3390/rs12233852.

[12] R. Raney, ‘Synthetic Aperture Imaging Radar and Moving Targets’, *IEEE Trans. Aerosp. Electron. Syst.*, vol. AES-7, no. 3, pp. 499–505, May 1971, doi: 10.1109/TAES.1971.310292.

[13] V. C. Chen, Fayin Li, Shen-Shyang Ho, and H. Wechsler, ‘Micro-doppler effect in radar: phenomenon, model, and simulation study’, *IEEE Trans. Aerosp. Electron. Syst.*, vol. 42, no. 1, pp. 2–21, Jan. 2006, doi: 10.1109/TAES.2006.1603402.

[14] X. Li, B. Deng, Y. Qin, H. Wang, and Y. Li, ‘The Influence of Target Micromotion on SAR and GMTI’, *IEEE Trans. Geosci. Remote Sens.*, vol. 49, no. 7, pp. 2738–2751, Jul. 2011, doi: 10.1109/TGRS.2011.2104965.

[15] M. Ruegg, E. Meier, and D. Nuesch, ‘Vibration and Rotation in Millimeter-Wave SAR’, *IEEE Trans. Geosci. Remote Sens.*, vol. 45, no. 2, pp. 293–304, Feb. 2007, doi: 10.1109/TGRS.2006.887025.

[16] F. Biondi, P. Addabbo, C. Clemente, S. L. Ullo, and D. Orlando, ‘Monitoring of Critical Infrastructures by Micro-Motion Estimation: the Mosul Dam Destabilization’, 2020, *arXiv*. doi: 10.48550/ARXIV.2007.05326.